Designing a light fabric metamaterial being highly macroscopically tough under directional extension: first experimental evidence

Francesco Dell'Isola, Tomasz Lekszycki, Marek Pawlikowski, Roman Grygoruk, Leopoldo Greco

Designing a light fabric metamaterial being highly macroscopically tough under directional extension: first experimental evidence

Francesco dell'Isola · Tomasz Lekszycki · Marek Pawlikowski · Roman Grygoruk and Leopoldo Greco

Abstract. In this paper, we study a metamaterial constructed with an isotropic material organized following a geometric structure which we call pantographic lattice. This relatively complex fabric was studied using a continuous model (which we call pantographic sheet) by Rivlin and Pipkin and includes two families of flexible fibers connected by internal pivots which are, in the reference configuration, orthogonal. A rectangular specimen having one side three times longer than the other is cut at 45° with respect to the fibers in reference configuration, and it is subjected to large-deformation plane-extension bias tests imposing a relative displacement of shorter sides. The continuum model used, the presented numerical models and the extraordinary advancements of the technology of 3D printing allowed for the design of some first experiments, whose preliminary results are shown and seem to be rather promising. Experimental evidence shows three distinct deformation regimes. In the first regime, the equilibrium total deformation energy depends quadratically on the relative displacement of terminal specimen sides: Applied resultant force depends linearly on relative displacement. In the second regime, the applied force varies nonlinearly on relative displacement, but the behavior remains elastic. In the third regime, damage phenomena start to occur until total failure, but the exerted resultant force continues to be increasing and reaches a value up to several times larger than the maximum shown in the linear regime before failure actually occurs. Moreover, the total energy needed to reach structural failure is larger than the maximum stored elastic energy. Finally, the volume occupied by the material in the fabric is a small fraction of the total volume, so that the ratio weight/resistance to extension is very advantageous. The results seem to require a refinement of the used theoretical and numerical methods to transform the presented concept into a promising technological prototype.

Keywords. Metamaterials · Failure toughness · Pantographic structures · Second-gradient models.

1. Introduction

The aim of this paper is to see how the continuum model formulated in [54,67] for fabrics constituted by inextensible fibers having bending energy can be used for designing some innovative metamaterials. The pioneering works by Pipkin and Rivlin [54–59,65–67,83] were motivated by clearly conceivable technological applications, but their impact was limited, in our opinion, by two circumstances: (i) Their models did produce mathematical problems which were too difficult to be solved in closed form and (ii) the physical systems which they considered were too difficult to built with the then available technology, and therefore, their study could not immediately lead to the production of any technologically relevant textures or materials. The impressive development of numerical technologies did drastically change, recently, the situation. First of all, the computing tools and the development of easy-to-use software did allow for the solution of otherwise unsolvable mathematical problems. Secondly, the advent of 3D printing made possible the realization of microscopically complex mechanical systems and therefore the realization of more advanced fabric materials.

The system which we want to consider here is constituted (see Figs. 1, 4) by two families of beams (or fibers with bending stiffness) which are printed in two arrays one orthogonal to the other, paralleling the same plane in which their motion will be assumed to be constrained. In the reference configuration, these two arrays are printed slightly displaced along the normal of their (parallel) planes and they are

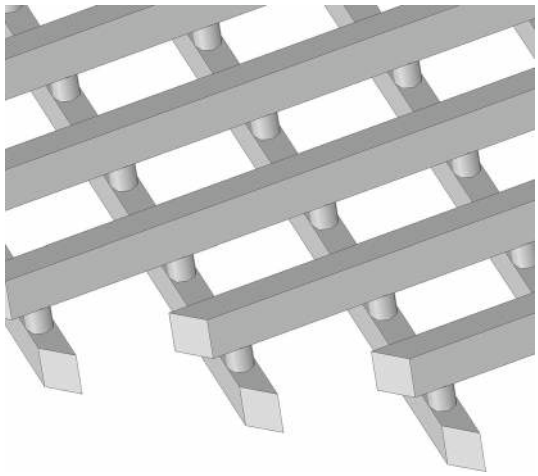

FIG. 1. Geometry of the 3D printed fabric

interconnected by some cylinders whose bases are circular and integral with the bottom or upper face of the fibers to which they are attached (see again Fig. 1).

These cylinders form an array of elastic pivots, whose elastic energy determines the shear deformation energy of the pantographic sheet, while the bending energy of fibers will produce a second-gradient effect in the continuum model deformation energy (see [19,34,35,83] or [16,17]). This system has a microstructure which seems suitably described by the aforementioned continuum models when second-gradient deformation energies are taken into account considered: In particular, the deformation energy has to account for the so-called geodesic bending [81].

The equilibrium of pantographic sheets is considered in the case of bias extension test with imposed elongation (hard device tests) along the direction of the shorter sides. The imposed relative displacement of shorter sides (see tensile tests shown in Fig. 4) is assumed to be such that the deformation of the specimen is doubly symmetric respect to its two principal referential inertia axes. The actual equilibrium shapes, the total deformation energy and the resultant forces applied by the hard device are estimated using Pipkin continuum models via a numerical code minimizing energy as functions of the imposed displacement. Different shear deformation and bending energies are postulated, and they are fitted with the first experimental evidence which were made available.

Remark that the pantographic lattices considered in the present paper may have a relevance also in the context of phenomena involving wave propagation, as shown by the investigation presented in [1,42,45,61]: It is indeed likely that macroscopic effects of the microstructure in pantographic fabrics may include frequency filtering and/or energy trapping. This aspect of the mechanics of these fabrics will be the subject of future investigations. Also very relevant may be the implications of the results presented here on the understanding of the biomechanics of living tissues: Indeed (see e.g., [26,31–33] and [36–38]), the role of fiber reinforcements on the mechanical behavior of growing and reconstructed tissues is attracting some attention. Finally, the consideration of multiphysics effects (as for instance piezo- or flexo-electricity) in systems having the geometry and the kinematics of a pantographic sheet can also disclose new possibilities (see [20,27]).

2. Pipkin continuum model for considered fabric

In this sections, we sketch the formulation of the Pipkin continuum model which has been used for formulating the models used in the elastic regime. For more details, the reader is referred to [16]. The

reader is warned: no attempt is made here to model damage and failure phenomena. This challenge has to be confronted, following the ideas presented in [68–70] suitably adapted to the context of second-gradient materials as done in [43,60,64]. Another consideration is needed here: In the present work, we do not try to derive the used continuum model by means of a homogenization procedure. Of course this micro–macro procedure is needed, and following the ideas presented, for example, in [2,3,77], in [6–8,18,28,62,71,72] in [10] or in [48–50] will be the object of further investigations (see also [63] for a general overview on generalized continua).

Let us consider the set of material particles of the introduced 2D continuum B embedded in the Lagrangian space $\mathcal{E}_{\mathcal{L}}$. The continuum B is meant to model the considered (and printed) pantographic sheet. We introduce an orthonormal system $(\mathcal{O}, X_1, X_2)$ in $\mathcal{E}_{\mathcal{L}}$ to label material particles. The sides of the considered specimen are assumed to be parallel to the introduced coordinate lines (see Fig. 2).

In every actual configuration, each material particle is placed, by a map $\mathbf{r}$, into positions belonging to the Eulerian space $\mathcal{E}$:

$$B \xrightarrow{\mathbf{r}} \mathbf{r}(B) \subseteq \mathcal{E}.$$

In order to model the printed specimens, we assume that B is a rectangle whose sides have length l and L, specified as follows:

$$B = \left\{ (X_1, X_2) \in \mathcal{E}_{\mathcal{L}} : \; X_1 \in [0, L] \,, \; X_2 \in \left[-\frac{l}{2}, \frac{l}{2} \right] \right\}.$$

We explicitly observe that the length ratio plays a relevant role: Here, we consider standard bias test, i.e., the case in which $L = 3l$. To take into account the material properties related to inextensibility, it is needed to introduce an adapted orthogonal reference system, $(\mathcal{O}, \xi_1, \xi_2)$, (called the *fiber reference*) which is oriented according to the directions of the inextensible fibers and which uses dimensionless space coordinates as follows:

$$\xi_1 := \frac{1}{l}(X_1 - X_2) + \frac{1}{2}, \qquad \xi_2 := \frac{1}{l}(X_1 + X_2) + \frac{1}{2}. \tag{1}$$

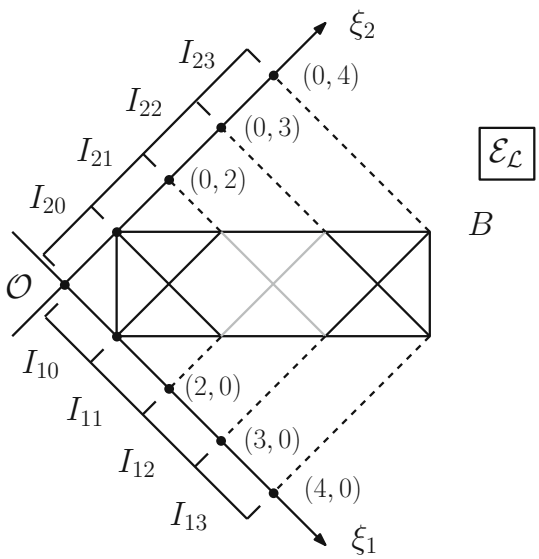

FIG. 2. Material (Lagrangian) coordinates adapted to inextensible fibers configuration

On occurrence, one can use the coordinates (ξ_1, ξ_2) to label a generic material particle of B and indicate with $\mathbf{D}_1(\xi_1, \xi_2)$ and $\mathbf{D}_2(\xi_1, \xi_2)$ the unit vectors tangent to the two families of fibers in the reference configuration at point (ξ_1, ξ_2).

2.1. Inextensibility and consequent representation of admissible placements

Let $\gamma \subset B$ be a rectifiable curve whose length is l: We say that γ is inextensible for an admissible placement $\mathbf{r}$ of B if for every arc α of γ, we have that $\mathbf{r}(\alpha)$ has the same length as α. In the present work, we will simply assume that the placement field $\mathbf{r}$ is piecewise-twice continuously differentiable in B. If we indicate with $\mathbf{F}$ the gradient of $\mathbf{r}$ in the points where it is defined, we get obviously that

$$\mathbf{d}_1 = \mathbf{F} \cdot \mathbf{D}_1, \qquad \mathbf{d}_2 = \mathbf{F} \cdot \mathbf{D}_2. \tag{2}$$

where the two vectors $\mathbf{d}_1$ and $\mathbf{d}_2$ represent the directions of the fibers in the current configuration, while the inextensibility constraint implies that a placement field of class C^1 in the neighborhood of a material particle P, verify the equalities:

$$\|\mathbf{F} \cdot \mathbf{D}_1\|^2 = \|\mathbf{d}_1\|^2 = \|\mathbf{F} \cdot \mathbf{D}_2\|^2 = \|\mathbf{d}_2\|^2 = 1. \tag{3}$$

Rivlin, in [67], proves that when $\mathbf{r} \in C^2(\Delta)$, where Δ is an open simply linearly connected subset of B, the inextensibility of the fibers implies that it is possible to find a particular representation of the placement field: There exist two vector fields $\mathbf{r}_1^{(\Delta)}(\xi_1)$ and $\mathbf{r}_2^{(\Delta)}(\xi_2)$, respectively, defined on the projection of Δ on the fiber axes ξ_1 and ξ_2 such that

$$\mathbf{r}_{(\Delta)}(\xi_1, \xi_2) = \mathbf{r}_1^{(\Delta)}(\xi_1) + \mathbf{r}_2^{(\Delta)}(\xi_2). \tag{4}$$

We can represent these two vector fields in the basis $(\mathbf{D}_1, \mathbf{D}_2)$ as follows:

$$\begin{cases} \mathbf{r}_1^{(\Delta)}(\xi_1) = \mu_1^{(\Delta)}(\xi_1)\,\mathbf{D}_1 + \nu_1^{(\Delta)}(\xi_1)\,\mathbf{D}_2 \\ \\ \mathbf{r}_2^{(\Delta)}(\xi_2) = \nu_2^{(\Delta)}(\xi_2)\,\mathbf{D}_1 + \mu_2^{(\Delta)}(\xi_2)\,\mathbf{D}_2, \end{cases} \tag{5}$$

being $\mu_1^{(\Delta)}, \mu_2^{(\Delta)}, \nu_1^{(\Delta)}, \nu_2^{(\Delta)}$ suitably regular scalar functions on the projections of Δ on the fiber axes ξ_1 and ξ_2.

It is easy to check that:

$$\exists \vartheta_1(\xi_1) : \ \mathbf{F} \cdot \mathbf{D}_1 = \cos(\vartheta_1(\xi_1))\,\mathbf{D}_1 + \sin(\vartheta_1(\xi_1))\,\mathbf{D}_2$$
$$\exists \vartheta_2(\xi_2) : (\forall \xi_2 \in) \ \mathbf{F} \cdot \mathbf{D}_2 = \sin(\vartheta_2(\xi_2))\,D_1 + \cos(\vartheta_2(\xi_2))\,\mathbf{D}_2$$

It is also easy to verify from the previous equations that, on any subdomain Δ whose points can be connected with segments parallel to ξ axes, the whole displacement field is known in terms of only two real functions of one real variable. Indeed once, for instance, the functions $\mu_1^{(\Delta)}$ and $\mu_2^{(\Delta)}$ are chosen, then the functions $\nu_1^{(\Delta)}$ and $\nu_2^{(\Delta)}$ are simply obtained via integration in terms of the functions $\mu_1^{(\Delta)}$ and $\mu_2^{(\Delta)}$ plus some integration constants (to be determined via suitable boundary conditions).

2.2. Imposed boundary conditions

The two segments Σ_1 and Σ_2 characterized, respectively, by the conditions (the short sides of the specimen)

$$X_1 = 0,\ X_2 \in \left[-\frac{l}{2}, \frac{l}{2}\right]; \quad X_1 = L,\ X_2 \in \left[-\frac{l}{2}, \frac{l}{2}\right]$$

are described, in the fiber reference, by the following other conditions:

$$\Sigma_1 := \{(\xi_1, \xi_2) \in B : \ \xi_1 \in [0,1], \xi_2 = 1 - \xi_1\}, \tag{6}$$

$$\Sigma_2 := \{(\xi_1, \xi_2) \in B : \ \xi_1 \in [3,4], \xi_2 = 7 - \xi_1\}. \tag{7}$$

In extension symmetric bias test, we impose the following boundary conditions on the two subsets Σ_1 and Σ_2 of the boundary of B:

1. vanishing displacement of the side Σ_1,
2. imposed displacement $\mathbf{u}_0 = u_0 \frac{(\mathbf{D}_1+\mathbf{D}_2)}{||(\mathbf{D}_1+\mathbf{D}_2)||}$ of the side Σ_2.

As already remarked in [54,67], because of inextensibility, the boundary conditions determine the placement field not only at the boundary but also in some regions inside the continuum at which they are applied.

2.3. Placement field in Δ_{00} and Δ_{33} and integral conditions implied by boundary conditions

The chosen boundary conditions on Σ_1 and Σ_2, imply that $\mathbf{r}$ is piecewise-two times differentiable in the regions delineated in Fig. 3 and equal to the identity on Δ_{00} and a translation in Δ_{33} (for the proof the reader is referred to [16]).

In Δ_{00}, we have that

$$\mathbf{r}(\xi_1, \xi_2) = \xi_1 \mathbf{D}_1 + \xi_2 \mathbf{D}_2 \tag{8}$$

while in Δ_{33}, we get:

$$\mathbf{r}(\xi_1, \xi_2) = (\xi_1 + u_{01}) \mathbf{D}_1 + (\xi_2 + u_{02}) \mathbf{D}_2 \tag{9}$$

Moreover, the continuity conditions in $P_i = (1,1)$ and $P_f = (3,3)$ of the placement field can be written as (see again [16]):

$$\begin{cases} \mu_1(3) + \int_1^3 \sin(\vartheta_2(\eta))\, \mathrm{d}\eta = 3 + u_{01} \\ \\ \mu_2(3) + \int_1^3 \sin(\vartheta_1(\eta))\, \mathrm{d}\eta = 3 + u_{02} \end{cases} \tag{10}$$

This condition imposes the continuity of the translation imposed to Δ_{33} with the displacement of the contiguous domains. By recalling that $(i = 1, 2)$

$$\frac{\mathrm{d}\mu_i(\xi_i)}{\mathrm{d}\xi_i} - \cos(\vartheta_i(\xi_i)) = 0, \ \mu_i(1) = 1, \tag{11}$$

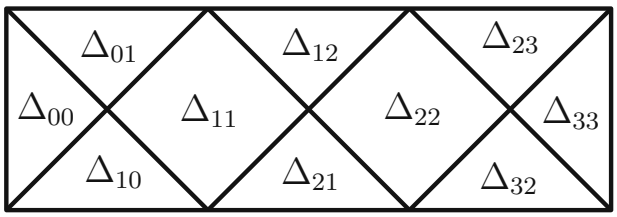

FIG. 3. Domains pattern imposed by boundary conditions

it is easy to express the found integral conditions exclusively in terms of the fields $\vartheta_i(\xi_i)$ as follows

$$\begin{cases} \int_1^3 \left(\cos\left(\vartheta_1\left(\eta\right)\right) + \sin\left(\vartheta_2\left(\eta\right)\right)\right) \mathrm{d}\eta = 2 + u_{01} \\ \\ \int_1^3 \left(\cos\left(\vartheta_2\left(\eta\right)\right) + \sin\left(\vartheta_1\left(\eta\right)\right)\right) \mathrm{d}\eta = 2 + u_{02}. \end{cases} \tag{12}$$

This form will be useful when looking for the equilibrium shapes of considered body by minimizing the deformation energy in hard devices tests.

2.4. Symmetric placements in considered bias extension tests

In this paper, we will consider, for considered specimen, only placements symmetric with respect to the X_1 axis. This means that given a point P of coordinates (ξ, η) and its symmetric P_s having coordinates (η, ξ), the following conditions hold:

$$\begin{cases} \mathbf{d}_1\left(P\right) \cdot D_1 = \mathbf{d}_2\left(P_s\right) \cdot D_2 \\ \\ \mathbf{d}_1\left(P\right) \cdot D_2 = \mathbf{d}_2\left(P_s\right) \cdot D_1 \end{cases} \Longrightarrow \begin{cases} \mu_{1,1}\left(\xi\right) = \mu_{2,2}\left(\xi\right) \\ \\ \nu_{1,1}\left(\xi\right) = \nu_{2,2}\left(\xi\right) \end{cases} \tag{13}$$

Considering the symmetry of boundary conditions and the first equality in (13), we derive directly the following identities:

$$\mu\left(\xi\right) := \mu_1\left(\xi\right) = \mu_2\left(\xi\right) \quad \vartheta\left(\xi\right) := \vartheta_1\left(\xi\right) = \vartheta_2\left(\xi\right) \quad \forall \xi \in \left[0, 4\right]. \tag{14}$$

Therefore, considering the relation between μ and ν, the kinematics of the problem is completely described by means of a unique field.

2.5. The space of configurations for 2D continua with two families of inextensible fibers in symmetric plane motion

If we assume the hypothesis of symmetry just described, the placement of B is completely determined by one scalar field $\mu\left(\xi\right)$ only, defined in the real interval $[0, 4]$. Because of the considered boundary conditions, recalling (8) and (9), μ has to be determined only in the interval $I = [1, 3]$. Thanks to (10) we have also the conditions

$$\mu\left(1\right) = 1, \qquad \mu\left(3\right) + \int_1^3 \sin\left(\vartheta\left(\eta\right)\right) \mathrm{d}\eta = 3 + u_0, \tag{15}$$

or equivalently the conditions

$$\mu\left(1\right) = 1, \qquad \int_1^3 \left(\cos(\vartheta\left(\eta\right)) + \sin\left(\vartheta\left(\eta\right)\right)\right) \mathrm{d}\eta = 2 + u_0. \tag{16}$$

The space of (admissible) configurations for 2D continua with two families of inextensible fibers (whose tangent vectors are orthogonal in the reference configuration) in plane motion is given by the set of pairs of fields (μ, ϑ) both defined in the interval $[1, 3]$. The field $\mu\left(\xi\right)$ is piecewise C^2, and the field $\vartheta\left(\xi\right)$ is piecewise C^1 with possible discontinuities in the point $\xi = 2$. The pairs of fields (μ, ϑ), together with the conditions (16), verify the local condition

$$\frac{\mathrm{d}\mu(\xi)}{\mathrm{d}\xi} - \cos\left(\vartheta\left(\xi\right)\right) = 0 \quad \forall \xi \in \left[1, 3\right]. \tag{17}$$

2.6. Constrained minimization of deformation energy

Once the deformation energy in terms of the shear deformation is introduced, we are reduced to the solution of a standard constrained optimization problem in which our energy functional, which depends only on the field ϑ, represents the objective function with inequality constraints on the angles fields (a condition of non-overlapping fibers) and the integral constraints on the angle filed imposed by boundary conditions. In formulas:

$$\begin{aligned} &\min_{(\vartheta)} \quad \mathfrak{F}(\vartheta) := \int_B W\left(\vartheta(\xi_1), \vartheta(\xi_2), \frac{\mathrm{d}\vartheta(\xi_1)}{\mathrm{d}\xi_1}, \frac{\mathrm{d}\vartheta(\xi_2)}{\mathrm{d}\xi_2}\right) \mathrm{d}B \quad \text{(Objective Function)} \\ &\text{subjectto:} \begin{cases} 0 < \vartheta(\xi_i) < \frac{\pi}{4}, \quad i = 1, 2., \quad \text{(Ineq. Constr.)} \\ \int_1^3 \cos(\vartheta(\xi_1))\mathrm{d}\xi_1 + \int_1^3 \sin(\vartheta(\xi_2))\mathrm{d}\xi_2 - 2 = u_0, \quad \text{(Eq. Constr.)} \\ \int_1^3 \cos(\vartheta(\xi_2))\mathrm{d}\xi_2 + \int_1^3 \sin(\vartheta(\xi_1))\mathrm{d}\xi_1 - 2 = u_0, \quad \text{(Eq. Constr.)} \end{cases} \end{aligned} \tag{18}$$

3. Numerical simulation in the elastic regimes

In this section, we exploit the Rivlin–Pipkin decomposition of plane displacement of continua with two families of inextensible fibers to find the equilibrium forms of a rectangular specimen having the inextensible fibers oriented at 45 ° with respect to the elongation direction. Indeed, the Rivlin–Pipkin decomposition allows for the formulation of a finite element integration scheme in terms of piecewise constant functions approximating the field ϑ : The fact that the integration scheme includes the inextensibility constraint without the need of introducing Lagrange multipliers makes the formulation of the algorithm much simpler and its convergence properties much easier to control.

The numerical simulations are based on some postulated expressions for the shear deformation energy: They are motivated *a posteriori* by comparison with the experimental data: The problem of deriving the most suitable one via a homogenization procedure (see e.g., [6,18,84,85]) is left for future investigations. The reader should, however, remark that in the present model, the different behaviors of the different mechanical parts which are constituting the elastic pivots (the cylinders which can be seen in Fig. 1) are described by the first-gradient (in displacement) dependence of the deformation energy density

$$W\left(\vartheta(\xi_1), \vartheta(\xi_2), \frac{\mathrm{d}\vartheta(\xi_1)}{\mathrm{d}\xi_1}, \frac{\mathrm{d}\vartheta(\xi_2)}{\mathrm{d}\xi_2}\right),$$

while the bending stiffness of involved fibers is taken into account via its second-gradient (in displacement!) dependence. Recall that because of (17), the dependence of W on ϑ implies a dependence on the first gradient of placement.

We manage to calculate exerted force as a function of imposed displacement by means of its expression based on Castigliano's first theorem: This information obtained from modeling procedure used is of experimental relevance.

One consideration is needed here: In the considered bias test (see Fig. 4), some specific deformation regions are delineated. In different regions, different (nearly constant in Lagrangian coordinates) shear deformation states are originated and some boundary layers separate these regions. Boundary layer location is determined clearly by imposed boundary conditions. On the other hand, their thickness and shape are mesh dependent when only first-gradient energies are considered. On the other hand, when second-gradient energies are assigned, then the consequent introduction of a characteristic length scale produces a model where also boundary layer thickness can be accounted for. The physical meaning of the newly considered length scale is easily associated with the ratio of bending and elongation stiffness of the fibers constituting the considered fabric.

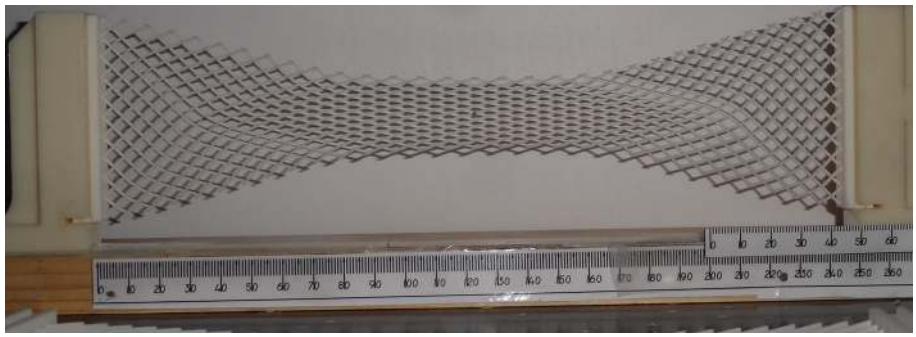

FIG. 4. Boundary layers

3.1. Description of the used numerical code

The minimization problem which we must solve involves the determination of a single real function of only one real variable.

This function is the angle field ϑ in terms of which, by means of the equation 17 (controllare che è buona la referenza!), the placement of considered 2D continuum is found. The integration scheme is conceptually very easy: We approximate the unknown field by a step function. The values of such a step function will be determined in order to minimize deformation energy.

The only difficulty to be confronted is represented by the fact that even if the total deformation energy is defined via a 2D integral, whose integrand function depends on two variables (i.e., the variables ξ_1 and ξ_2), such integrand function is defined in terms of the real variable function ϑ only. The reference configuration is therefore suitably partitioned into the union of rectangles inside of which the deformation energy is estimated by means of the corresponding values of the considered step function, while the total energy is simply estimated via Riemann sums. The considered constrained optimization problem is numerically solved by means of two solver: the **Nminimine** solver in Mathemathica® and the open source solver MIDACO[1] in C++ ambient that offers a very efficient parallelization strategy.

For making the computations more expeditive, the presented numerical simulations were performed for a mesh having 20×60 elements for the whole specimen.

3.2. Results of numerical simulations: equilibrium shapes and angle fields

A first result of the numerical simulations which we have performed concerns the determination of the shape of considered specimen in the case of imposed relative displacement of the two short sides of the considered rectangular body.

As discussed in Sect. 2, the first field which can be determined is the field of shear angles ϑ.

The numerical simulations performed in this paper used the four deformation energy densities listed below. Remark that the stiffness has been assumed to be equal to 1 when we considered only one of the listed energies in the simulations: Its value will play a role only in the determination of the value of exerted external forces needed to determine a given displacement. When the sum of the first and the forth energy is considered, then the stiffnesses α and β are introduced, respectively, for first- and second-gradient energies.

[1] $MIDACO - SOLVER$ (or Mixed Integer Distributed Ant Colony Optimization) can be downloaded from http://www.midaco-solver.com/; an overview on nonlinear optimization solvers can be founded in http://en.wikipedia.org/wiki/List_of_optimization_software.

1. Trigonometric first-gradient shear energy given by the following formula:

$$W_1^I(\vartheta) = \frac{1}{2}\sin^2\vartheta$$

2. Quadratic first-gradient shear energy:

$$W_2^I(\vartheta) = \frac{1}{2}\vartheta^2$$

3. Quadratic first-gradient shear energy

$$W_3^I(\vartheta) = \frac{1}{2}\vartheta^4$$

4. Quadratic second-gradient energy

$$W_1^{II}(\vartheta) = \frac{1}{2}\left(\nabla\vartheta\right)^2.$$

The results of numerical simulations allow us to remark that for a first-gradient shear energy model:

- the shear angle field in general is not constant with respect to Lagrange coordinates (see Fig. 5a, c where W_1^I has been used);
- there is at least one energy density for which there exists a relative displacement for which the equilibrium shear angle field is piecewise constant with respect to Lagrange coordinates (see Fig. 5b where W_1^I has been also used);
- for all the other energy densities considered the equilibrium shear angle field is never constant (with respect to Lagrange coordinates) for all imposed relative displacements (see Figs. 6, 7, where the energies W_2^I and W_3^I are considered);
- the maximum shear angle is not always located at the center of the specimen (see Fig. 5a).

In subsequent numerical simulations the energy density αW_1^I plus the second-gradient quadratic energy density βW_1^{II} (with ratio on the constitutive parameter 50:1) have been considered. The results which were obtained can be resumed as follows:

- the shear angle field in general is not constant with respect to Lagrange coordinates (see Fig. 8),
- because of the addition of second-gradient energy, the equilibrium shear angle field is not anymore constant for all imposed relative displacements,
- contrary to what happens when the energy W_1^I alone is considered, with suitably large coefficients for second-gradient energy, the maximum shear angle is always located at the center of the specimen (see Fig. 8),
- the introduction of second-gradient energy regularizes the field ϑ so that it does not suffer jumps at the separating curves of the Δ domains shown in Fig. 3.

After having calculated the field ϑ, the placement field can be consequently calculated via a standard integration process in one variable only. The shapes of the specimen, for the energy $\alpha W_1^I + \beta W_1^{II}$, obtained for the same imposed relative displacements and same parameter β, for several different values of the parameter α are shown in the Figs. 9 and 10. From these figures for increasing values of the parameter α, that weights the first-gradient shear energy W_1^I, one can show the transition from the shape characteristic of the second-gradient-dominated fabric (see Fig. 10) to those characterizing the first-gradient-dominated fabric. In these last shapes, one can verify the presence of the expected jumps in the ϑ fields (see Fig. 9).

A first examination of the calculated equilibrium shapes of considered specimen shows that many relevant features of the field ϑ depend on the postulated deformation energy. As a consequence, the phenomenological fitting of the deformation energy more suitable to describe a given specimen can be based on the consideration of the values assumed by the field ϑ in some more relevant material particles of the specimen. We have chosen the material points $(\xi_1 = 1, \xi_2 = 1)$ and $(\xi_1 = 2, \xi_2 = 2)$ (see Fig. 2) to estimate some values of ϑ particularly meaningful. In other words, we will consider the plots of the angles

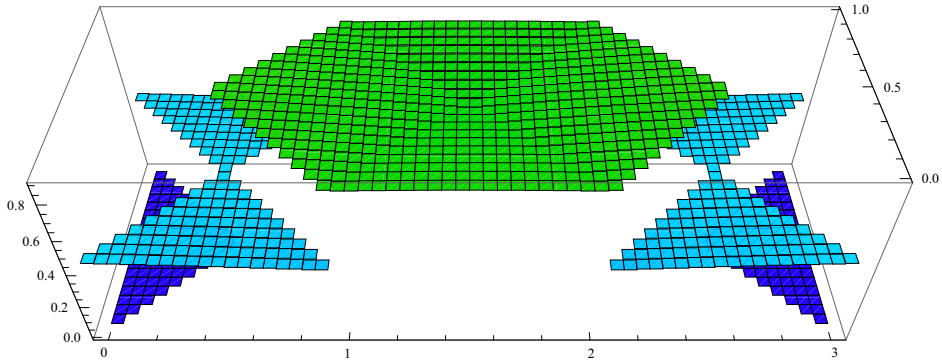

(a)

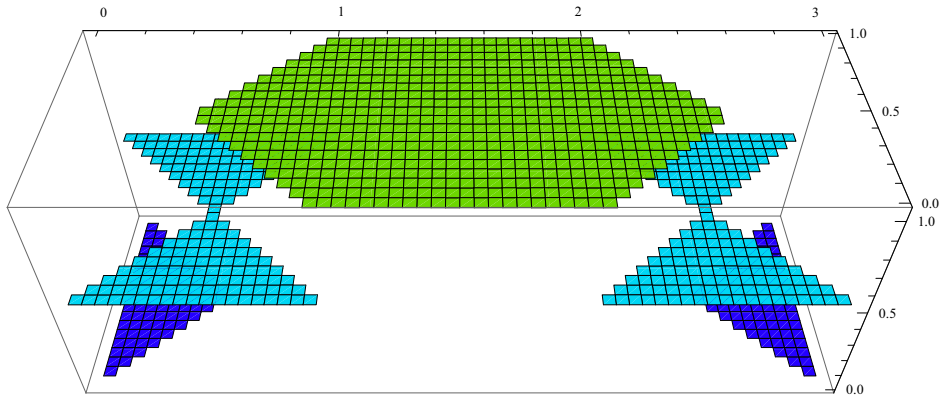

(b)

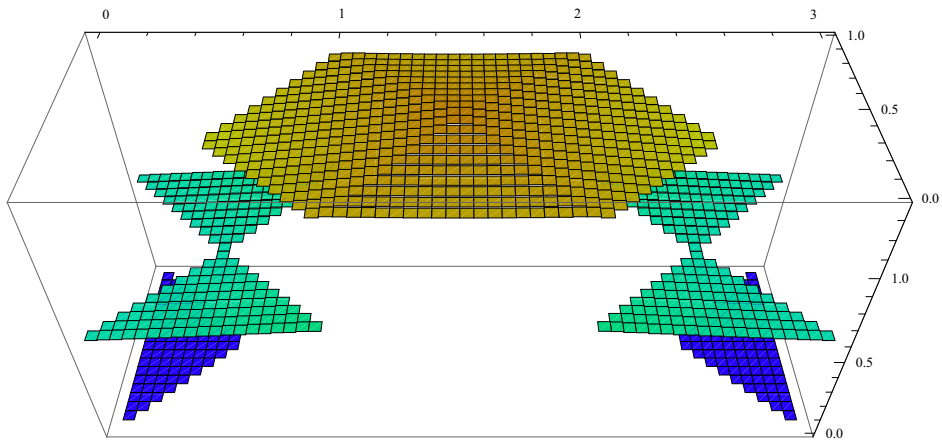

(c)

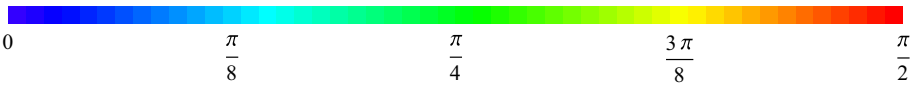

FIG. 5. Total angle $\vartheta_1 + \vartheta_2$ for several values of imposed relative displacement when W_1^I is used: **a** $u_x = u_y = 0.65 * L$, **b** $u_x = u_y = (\sqrt{3} - 1) * L$, **c** $u_x = u_y = 0.8 * L$

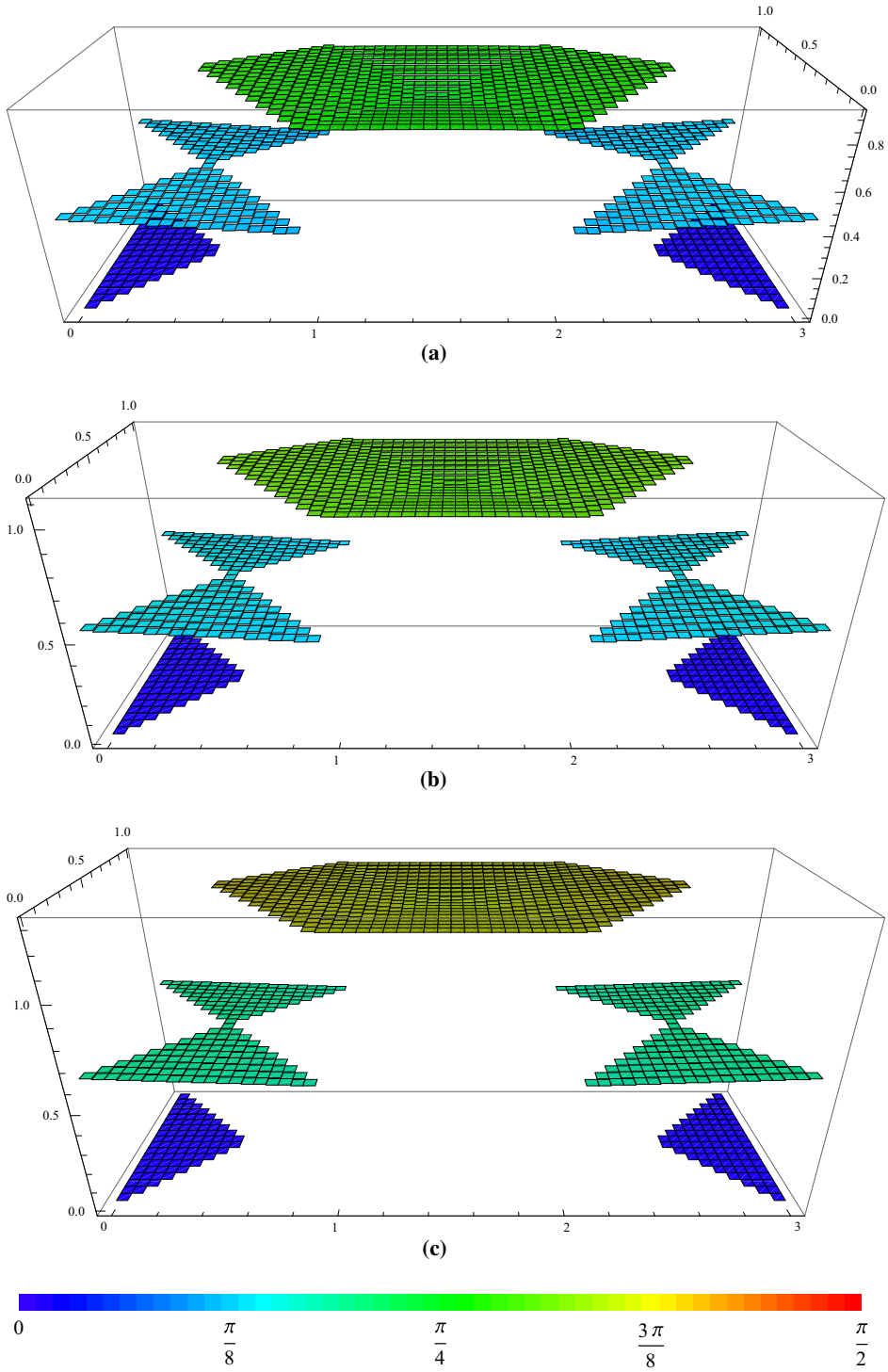

FIG. 6. Total angle $\vartheta_1 + \vartheta_2$ for several values of imposed relative displacement when W_2^I is used: **a** $u_x = u_y = 0.65 * L$, **b** $u_x = u_y = (\sqrt{3} - 1) * L$, **c** $u_x = u_y = 0.8 * L$

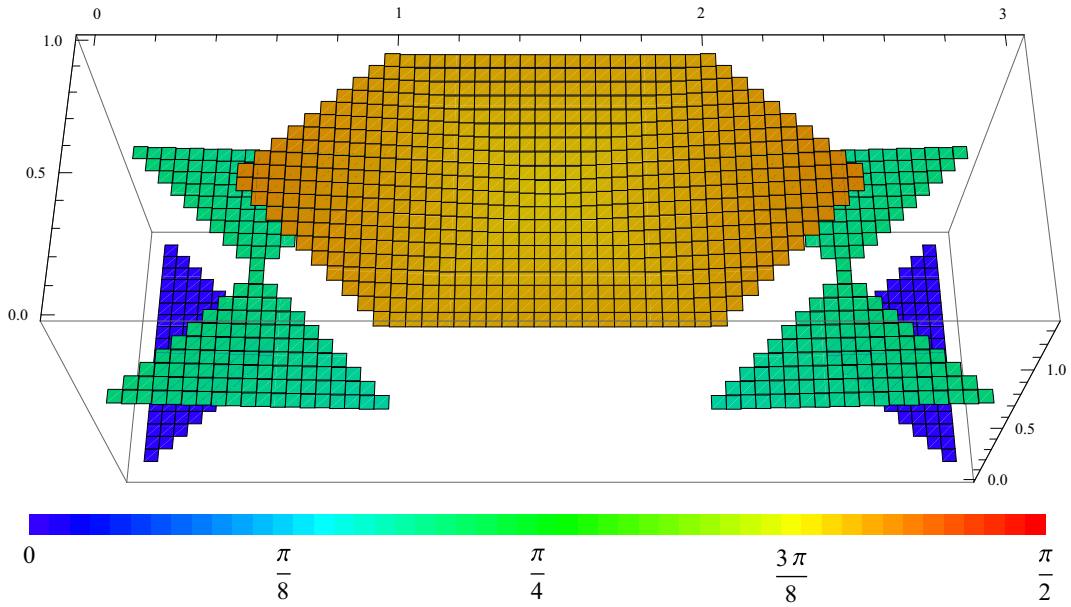

FIG. 7. Total angle $\vartheta_1 + \vartheta_2$ for several values of imposed relative displacement when W_3^I is used: $u_x = u_y = 0.8 * L$

$\vartheta_p := \vartheta(1,1)$ and $\vartheta_c := \vartheta(2,2)$ (and their difference) as functions of the imposed relative displacement when different deformation energies are postulated.

In Fig. 11, these energies are the quadratic one (dashed lines), i.e., $W_2^I(\vartheta)$, or the trigonometric one (continuous lines), i.e., $W_1^I(\vartheta)$, regularized with the same second-gradient quadratic energy W_1^{II}. The total energy is obtained via a linear combination of first- and second-gradient energies with different values for weighting coefficients α and β: Their considered values are indicated in the same figure.

It can be easily remarked that the trend of the plots for $\vartheta_p := \vartheta(1,1)$, $\vartheta_c := \vartheta(2,2)$ and their difference is qualitatively and quantitatively different in three specific ranges for the ratio α/β. The first range is when the second-gradient effects are dominating (see left plot in Fig. 11). One can then distinguish the transition range (see the central plot in Fig. 11) and finally the range where the first-gradient effects are dominating (see the right plot in Fig. 11).

The trends of the plots are rather different in the three previously identified ranges. In fact it has to be remarked that:

- in the range where second-gradient energy is dominating, the angle at the center of the specimen ϑ_c (green line) is smaller than the angle ϑ_p (blue line) at the corner p;
- in the transition range, the two angles have comparable values;
- in the range where the first-gradient energy is dominating, the angle at the center of the specimen ϑ_c (green line) is greater than the angle ϑ_p (blue line) at the corner p;
- the difference between the two angles (plotted by the red line) has a trend which can be adopted as an indicator to determine in which one of the three identified ranges it a specific specimen can be classified.

All above-listed considerations have directed the design of the performed experimental measurements, whose first preliminary results will be shown.

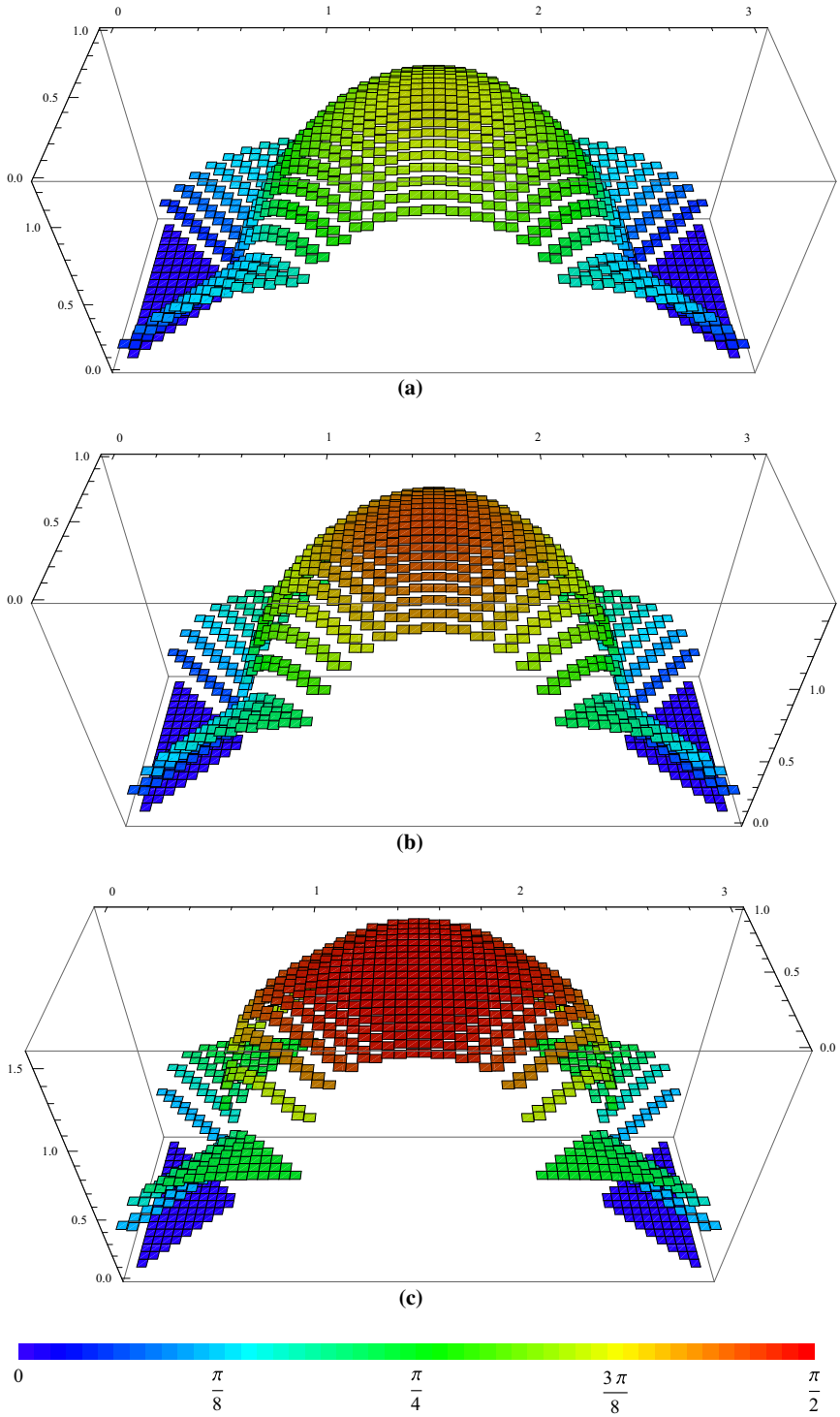

FIG. 8. Total angle $\vartheta_1 + \vartheta_2$ for the deformation energy $\alpha W_1^I + \beta W_1^{II}$ for several values imposed relative displacement: **a** $u_x = u_y = 0.65 * L$, **b** $u_x = u_y = (\sqrt{3} - 1) * L$, **c** $u_x = u_y = 0.8 * L$

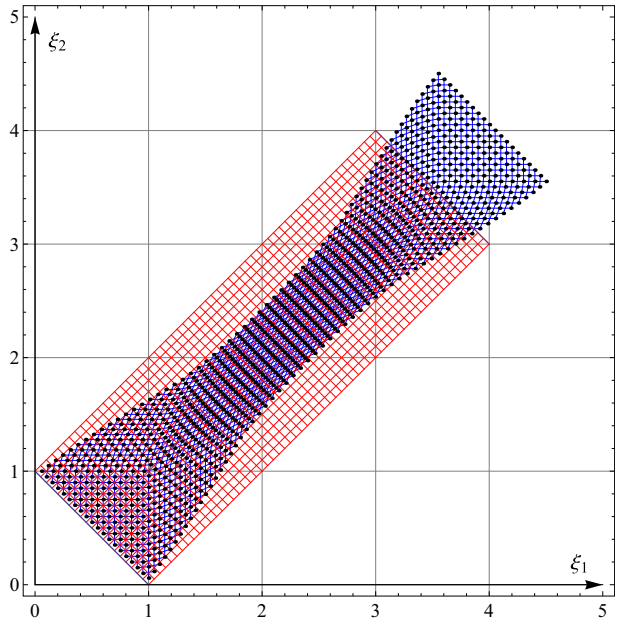

FIG. 9. Deformed configuration for $u_x = u_y = 0.6 * L$, $\alpha = 5$ and $\beta = 1$

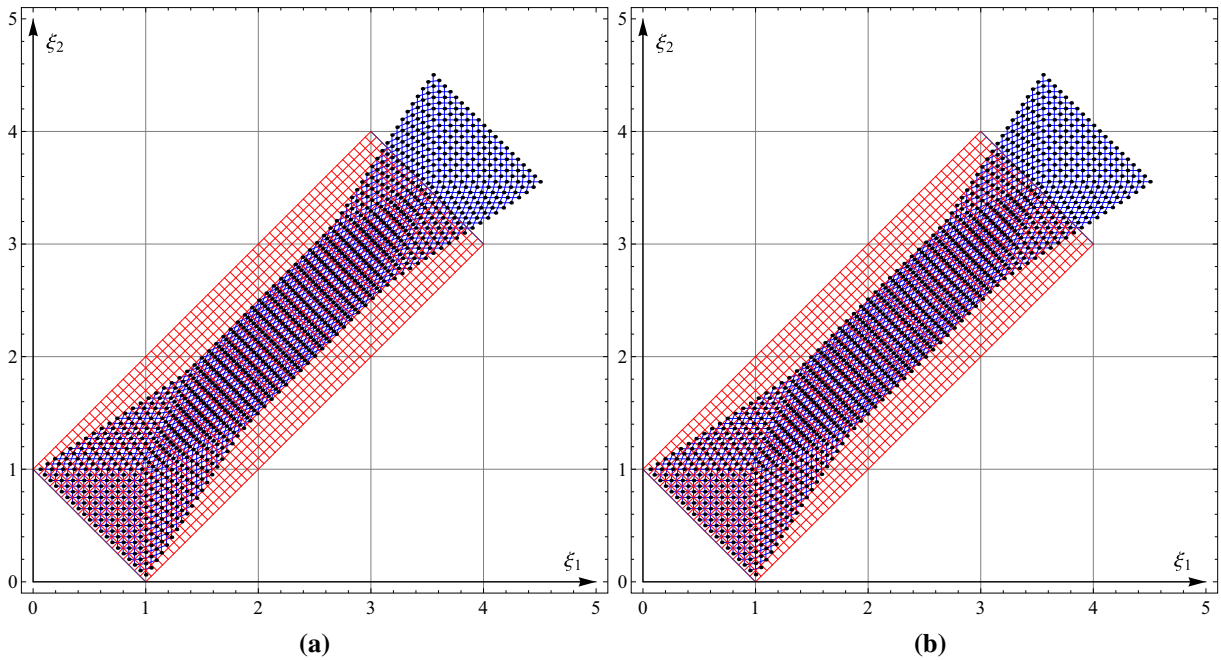

FIG. 10. Deformed configuration for $u_x = u_y = 0.6 * L$ and $\beta = 1$: **a** $\alpha = 25$ and **b** $\alpha = 50$

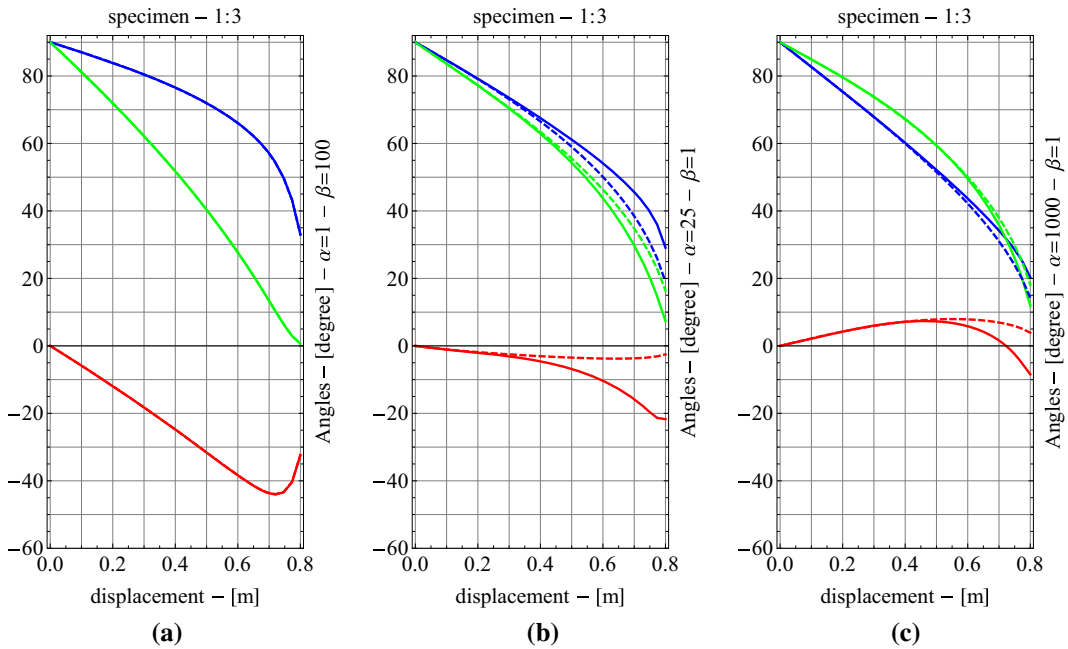

FIG. 11. Incremental angle behaviors for the first- and the second-gradient energy model

3.3. Exerted forces as functions of imposed displacements: dependence on the deformation energy density

In this section, we show how the total deformation energy in equilibrium configuration depends on imposed relative displacement. This estimate is of great importance in the applications, as the capability of considered fabric to resist to damage progress is obviously related to this physical quantity. Another important physical quantity to be taken into account in this context is the total external resultant force which must be applied to get a given relative displacement.

The numerical simulations show that the expression of the postulated deformation energy density influences how the equilibrium total energy depends on the imposed displacement. Because of the first Castigliano's theorem, the derivative of this equilibrium total energy supplies the applied external resultant force, which is shown in Fig. 12.

To be more specific in Fig. 12 are shown the curve relative displacement–external force for the first-gradient quadratic, quadratic and trigonometric first-gradient deformation energy and for the quadratic pure second-gradient deformation energy. We recall again that the considered model is exclusively elastic.

We also remark that in order to get a prediction of the stress concentrations in the fibers at the corners of the specimen, one should relax the inextensibility condition and test the equilibrium solution in a suitable virtual displacement. As a consequence, the present treatment does not allow for the introduction of the yield criteria needed to describe failure initiation. Postponing such a study to further developments, we remark that (see again Fig. 12) the resultant force increases (for pure geometric effects) when the specimen approaches the limit of maximum elongation allowed by inextensibility constraint.

4. Experimental evidence: macroscopic toughness in extension

The aim of the designed measurements campaign is to prove that the considered specimen, when the damage and rupture of microscopic structure due to pivot failure or fiber rupture start arising, still is able

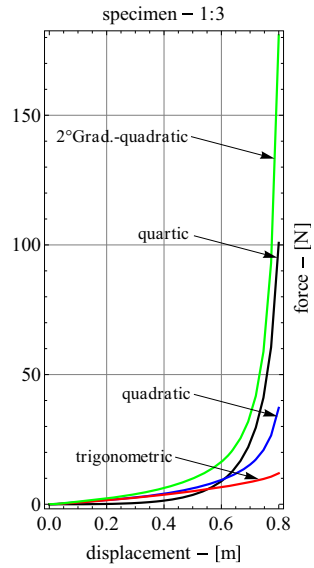

FIG. 12. Force–displacement curve for the considered energy model

to stand externally applied loads in a wide range. The observed experimental evidence will motivate the further development of mathematical and numerical models for considered fabric to include damage onset and development. The reader will find interesting, and relevant, experimental investigation involving fiber reinforcements for composites in the papers, [46,47,73–76] where also once set and progress of damaged is considered. In future investigations, the methods there used will be adapted to the present contest.

Moreover, the performed measurements have shown that in the displacements range starting from the first rupture up to the definitive failure and for some specific geometries of the microstructures, the energy required for reaching total rupture is greater than the amount of elastic energy which can be stored by the specimen. This suggests that the considered microfabric has the potentialities to supply an extremely tough metamaterial.

Three samples were tested. All of them contained the same beam cross-sectional dimensions, i.e., $1.2 \times 1.2\,\mathrm{mm}$. They differed only by the dimensions of the pivots that connected the beams. The pivots dimensions are presented in the table

Sample number	Pivot height [mm]	Pivot diameter [mm]
1	1.0	0.9
2	0.5	0.9
3	0.5	0.6

4.1. Description of specimen obtained by 3D printing

The specimen considered for the described experimental measurements was prepared by means of a 3D printer. The type is the printer FORMIGA P100 (EOS GmbH), the material used was PA 2200 (polyamide powder), and the software used to generate the 3D models of the specimens was SolidWorks. The geometry of the specimen was specified by means of the STL format files, which was used as an input by the 3D printer. In Fig. 13, details of the periodicity cell of printed pantographic specimen are shown.

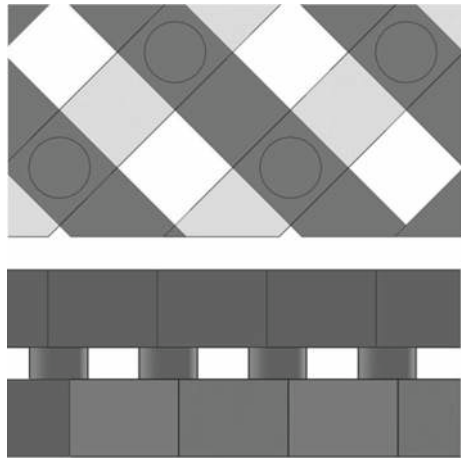

FIG. 13. Details of the pantographic specimens periodicity cell

4.2. Hard device and load cell used

The specimens were tested on the MTS Bionix System strength machine. The displacement was imposed with the velocity 20 mm/min. It is regulated by means of multipurpose TestSuite software which fully controls the machine activity. The exerted force was measured by means of MTS load unit which is an integral part of the machine. It is a strain gauge type, accurate in both dynamic and static tests. The unit comprises both axial and axial torsional force transducers. The force transducer measures the amount of tension or compression applied to it. It has four strain gauges that form a balanced Wheatstone bridge. When forces are applied to the bridge, it becomes unbalanced and produces an electrical signal that is proportional to the force applied to it.

4.3. Limits of inextensibility assumption: elongation measurements

The campaign of measurements has shown that there are some fibers which are remarkably elongated. Indeed, as seen in Figs. 14, 15 and 16, the fibers connected at the fixed corners of the specimen undergo a remarkable stress and strain solicitation. The initial measured fiber length was equal 20 mm. The curves in Figs. 14, 15 and 16 are drawn until the moment when the fiber was destroyed.

The reader should remark that:

- the beams (fibers) with two marks at the lower right-hand side corner in Figs. 17, 18 and 19 are subject to a large elongation between the pivots marked with black dots. Estimating the Young modulus of the used material as having the value 1900 MPa, the measured elongation (while estimating the area of the beam as having the value 1.44 mm^2: Poisson effect can be suitable taken into account) implies that the most solicited fibers are subjected to a traction stress states of approx. 200 MPa (sample 1 and 2) and 70 MPa (sample 3).
- the other beams are not undergoing large elongations, and the geometry of deformed specimen is well captured by the model based on inextensibility assumption.
- there are regions in which bending energy of fibers is concentrated: These regions are close to the fibers which are most elongating.
- It is therefore clear that an improvement in the presented and used model is required, even if it gives a reasonably accurate description of the global behavior of the fabric.

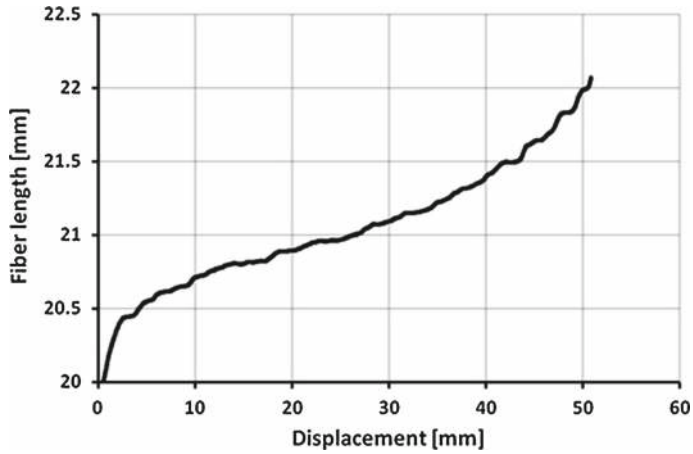

FIG. 14. Fiber length versus displacement curve registered during tensile test of sample 1

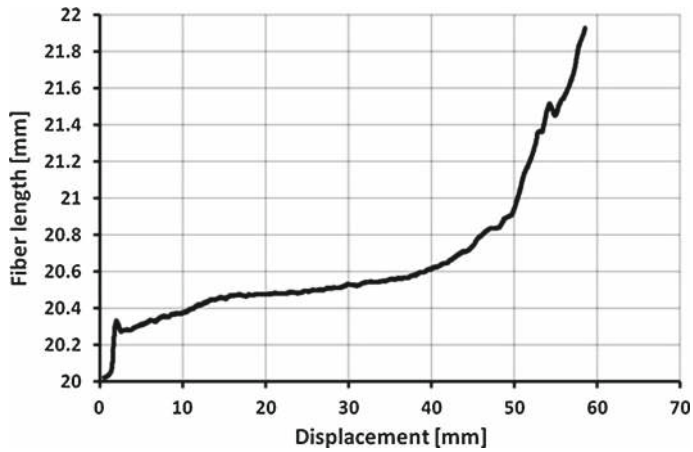

FIG. 15. Fiber length versus displacement curve registered during tensile test of sample 2

4.4. Shear angle measurements

This section refers to Figs. 17, 18 and 19 in which the angles between two close beams connected by an elastic pivot are shown by means of three marks patterned in triangle. The angles are placed in the lower parts of the samples where two characteristic beams meet and in the middle of the samples. It can be seen that those angles are not constant. A good estimate of these two angles, in the framework of the Pipkin's type models, is given by the theoretical values obtained in the previous section for the angles $\vartheta_p := \vartheta(1,1)$, $\vartheta_c := \vartheta(2,2)$. Figures 17, 18 and 19 show how different geometries of the pivots and beam sections are affecting these angles. This dependence and its role in the comprehension of the mechanical behavior of pantographic sheets will deserve a further investigation, both theoretical and experimental.

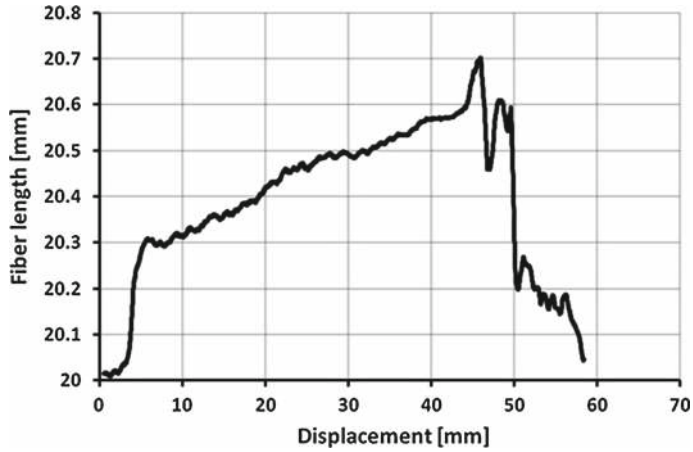

FIG. 16. Fiber length versus displacement curve registered during tensile test of sample 3

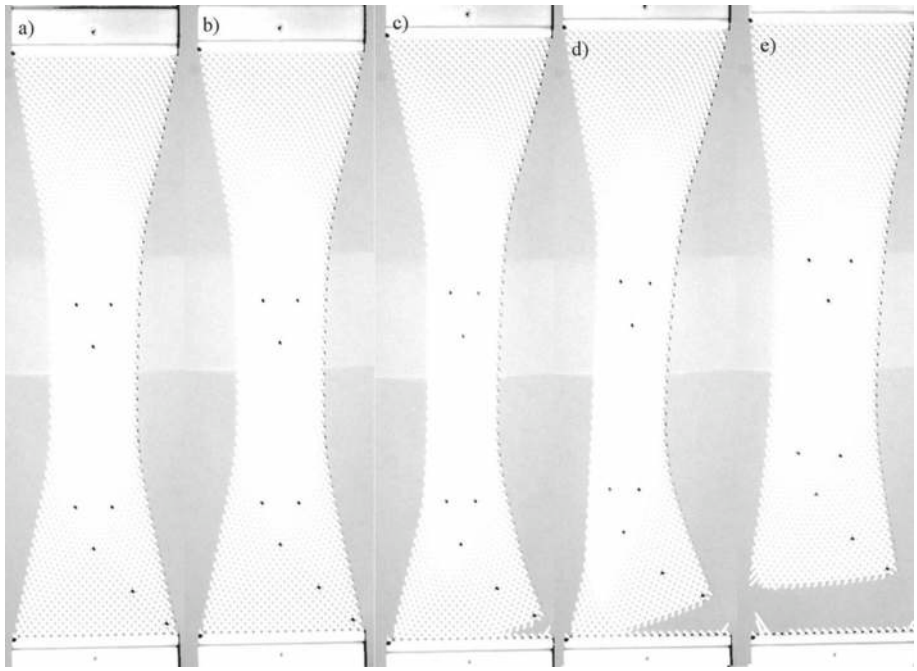

FIG. 17. Tensile test of sample 1 (see also Fig. 20)a) sample under stretch before first beam breakage, **b** fiber connected to the lower left-hand side corner deterioration, **c**, **d** damage of further fibers, **e** complete deterioration of the sample

4.5. Measured toughness in extension

Toughness of a material can be defined as the amount of energy needed to lead it to failure. The complex geometry of considered specimen is such that, while undergoing to large deformations and damage progression, the constituting beams reorganize themselves in order to show an increasing resistance to

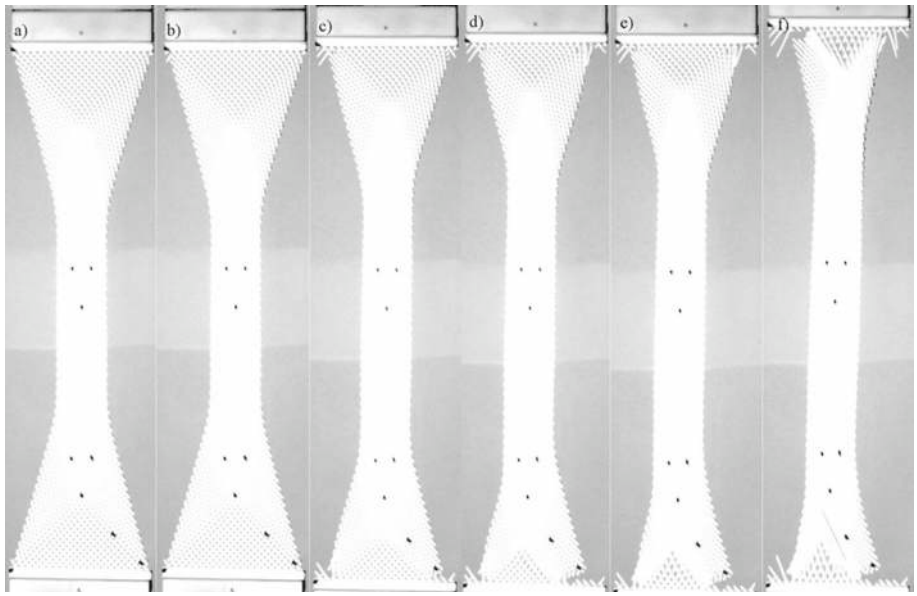

FIG. 18. Tensile test of sample 2 (see also Fig. 21): **a** sample under stretch before first beam breakage, **b** fiber connected to the upper left-hand side corner deterioration, **c**–**f** damage of further fibers

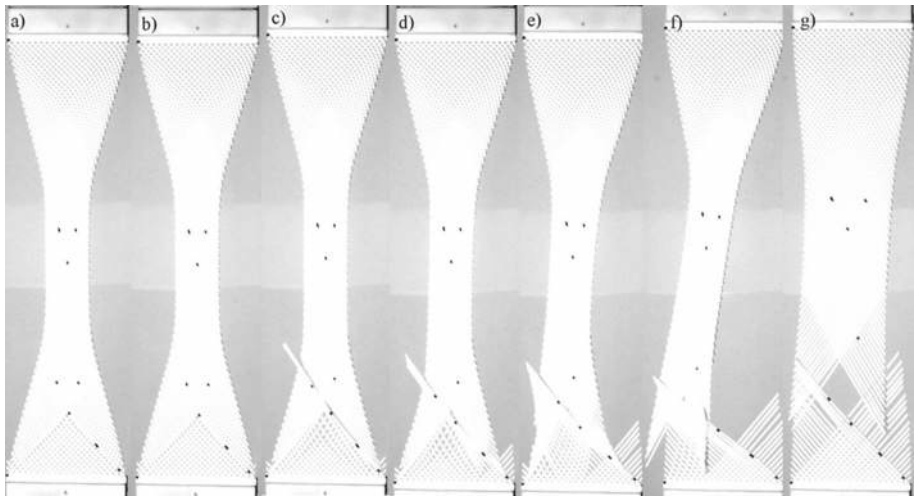

FIG. 19. Tensile test of sample 3 (see also Fig. 22): **a** sample under stretch before first beam breakage, **b** fiber connected to the lower right-hand side corner deterioration, **c**–**f** damage of further fibers, **g** complete deterioration of the sample

elongation, in the particular direction which we consider. This simple consideration explains the following experimental evidences (see Figs. 20, 21, 22). In the figures, characteristic points are depicted. Those points correspond to the pictures of the samples presented in Figs. 17, 18 and 19.

In Fig. 20, the force versus displacement curve for sample 1 is presented. The points in this curve correlate with the pictures in Fig. 17. Similarly, the points in Fig. 21 are related to the deformation of

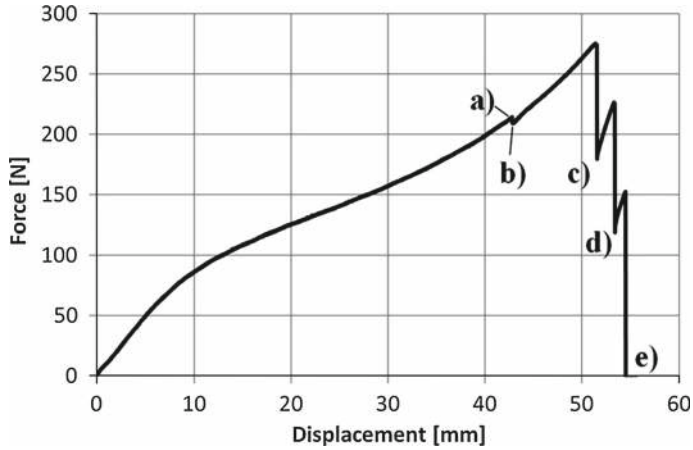

FIG. 20. Force versus displacement curve registered during tensile test of sample 1 with characteristic points corresponding to pictures in Fig. 17

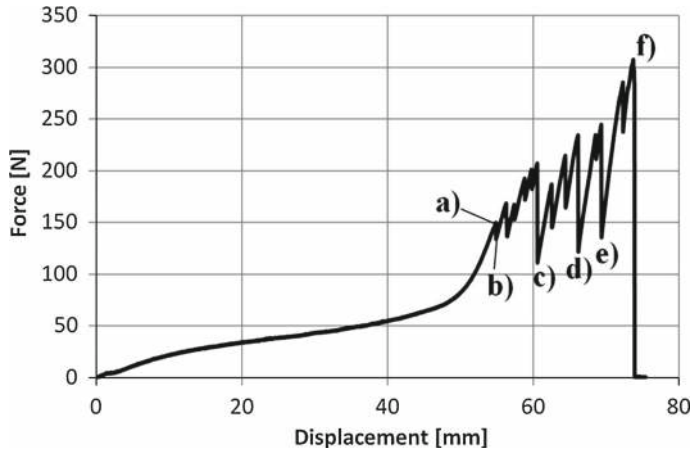

FIG. 21. Force versus displacement curve registered during tensile test of sample 2 with characteristic points corresponding to pictures in Fig. 18

sample 2 which is shown in Fig. 18. Finally, the characteristic points in Fig. 22 correspond to respective pictures in Fig. 19 which show consecutively deformation of sample 3.

5. Conclusions and perspectives

The mathematical continuum model developed in [16,17,81], based on the ideas originated by Rivlin and Pipkin, showed to be an useful tool for design of complex plane pantographic metamaterials. The order of magnitude of resultant forces in bias extension test (based on an intuitive micro–macro identification of deformation energy density) has been easily forecast, as well as, in a rather precise qualitative and quantitative way, the deformed shape, in large deformation, of considered specimen. The so-obtained theoretical knowledge allowed for the design of a first campaign of experimental measurements. The experimental

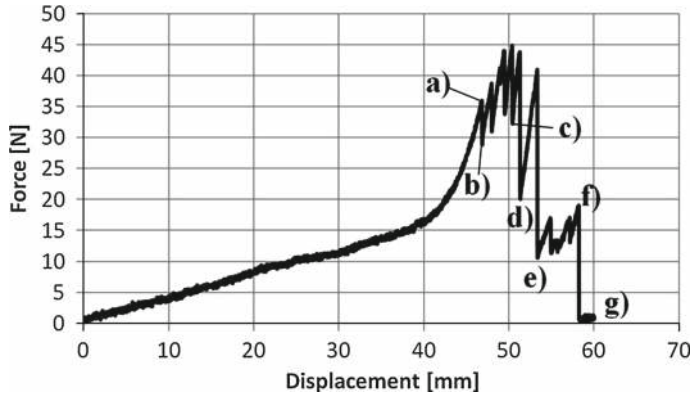

FIG. 22. Force versus displacement curve registered during tensile test of sample 3 with characteristic points corresponding to pictures in Fig. 19

evidence concerning the large elastic deformations of considered specimen and the subsequent failure, rupture and failure phenomena seem to be very promising. Indeed:

- when suitably optimizing the elastic pivot geometry and beam sections, the considered specimen, after the linear and nonlinear elastic regimes, shows a wide range of relative displacements and resultant forces in which, even if failure does not occur, damage is progressing;
- during the damage progression, the resultant force exerted increases reaching values which are several times greater than the force exerted at the end of the elastic regime;
- the total energy which the specimen can adsorb before reaching the final failure in the range of displacements characterizing damage progression is greater than the maximum of elastic energy which can be stored in the elastic regime;
- the specific weight of the fabric is relatively low, so that the mechanical performances of the specimen relative to their weight are really surprising.

One can conclude that the concept which we have presented in this paper deserves a closer investigation and may produce interesting and technologically relevant applications. The presented results show that it is needed to improve the used model in many directions. For instance, one could:

- Try to get some information about the state of stress of each single inextensible fiber in the framework of a slight generalization of presented Pipkin continuum model. This could be done by refining the application of Castigliano's first theorem by somehow relaxing the inextensibility condition to the fibers whose state of stress is to be determined. This could allow for the introduction of a yield criterion and a consequent description of the failure process, to be compared with the presented experimental evidence.
- Try to introduce a semi-discrete model for considered fabric in which each fiber is modeled as an Euler beam interconnected to the other fibers by elastic pivots, whose deformation energies can be calculated by separate numerical simulations based on 3D Cauchy continuum theory. This model should have the capability of better capturing the behavior of the considered fabric, as it is discrete in nature, for what concerns its pantographic geometry. However, this model may have some drawbacks, at the beam model applicability is not assured when the diameter of the beams sections is comparable with the distance between two consecutive pivots. In this respect, we underline that the so-called GBTs (Generalized Beam Theories) may be of use (see e.g., [39,51–53]) also for starting the study of dynamical behavior of pantographic sheets. Furthermore, these meso-models can be developed on the framework of the isogeometric analysis as in [11,12,29,30,82].

- Try to introduce a fully 3D Cauchy continuum model, by using the same geometrical files used for printing the fabric with the 3D printer. While such an approach is less challenging from a conceptual point of view, it shows formidable numerical difficulties, which need to be considered carefully. The perturbative analysis of 3D Cauchy continuum model to locate the regions of deformation concentration (see e.g., [14,40,41,51] and [9]) or to obtain reduced models (see e.g., [4,5,24,44,78–80]) seems an important conceptual tool to be exploited in this context. For other types of fiber configurations, the symmetry analysis performed in [22,23,25] may be useful for construction of the 2D or 3D strain energy densities within the framework of the generalized models of continua with directors. The occurrence of localization and eventual damage in the specimen is an issue of great relevance that deserves a specific attention and that might be modeled employing one of the methods that have been proposed for discontinuous displacement fields like in [13,15,21,86].

References

1. Abo-el Nour, N., Alshaikh, F., Giorgio, I., Della Corte, A.: A mathematical model for longitudinal wave propagation in a magnetoelastic hollow circular cylinder of anisotropic material under the influence of initial hydrostatic stress. Math. Mech. Solids (2015). doi:10.1177/1081286515582883
2. Alibert, J.J., Della Corte, A.: Second-gradient continua as homogenized limit of pantographic microstructured plates: a rigorous proof. Zeitschrift für angewandte Mathematik und Physik (2015). doi:10.1007/s00033-015-0526-x
3. Alibert, J.-J., Seppecher, P., dell'Isola, F.: Truss modular beams with deformation energy depending on higher displacement gradients. Math. Mech. Solids **8**(1), 51–73 (2003)
4. Altenbach, H., Eremeyev, V.A., Lebedev, L.P.: On the existence of solution in the linear elasticity with surface stresses. ZAMM-J. Appl. Math. Mech. **90**(3), 231–240 (2010)
5. Altenbach, H., Eremeyev, V.A., Lebedev, L.P.: On the spectrum and stiffness of an elastic body with surface stresses. ZAMM-J. Appl. Math. Mech. **91**(9), 699–710 (2011)
6. Assidi, M., Ben Boubaker, B., Ganghoffer, J.F.: Equivalent properties of monolayer fabric from mesoscopic modelling strategies. Int. J. Solids Struct. **48**(20), 2920–2930 (2011)
7. Andreaus, U., Giorgio, I., Madeo, A.: Modeling of the interaction between bone tissue and resorbable biomaterial as linear elastic materials with voids. J. Appl. Math. Phys. **66**(1), 209–237 (2015)
8. Berezovski, A., Giorgio, I., Della Corte, A.: Interfaces in micromorphic materials: wave transmission and reflection with numerical simulations. Math. Mech. Solids. (2015). doi:10.1177/1081286515572244
9. Bersani, A.M., Giorgio, I., Tomassetti, G.: Buckling of an elastic hemispherical shell with an obstacle. Contin. Mech. Thermodyn. **25**(2), 443–467 (2013)
10. Carcaterra, A., dell'Isola, F., Esposito, R., Pulvirenti, M.: Macroscopic description of microscopically strongly inhomogenous systems: a mathematical basis for the synthesis of higher gradients metamaterials. Arch. Ration. Mech. Anal. 1–24 (2015). doi:10.1007/s00205-015-0879-5
11. Cazzani, A., Malagù, M., Turco, E.: Isogeometric analysis of plane-curved beams. Math. Mech. Solids (2014). doi:10.1177/1081286514531265
12. Cazzani, A., Malagù, M., Turco, E.: Isogeometric analysis: a powerful numerical tool for the elastic analysis of historical masonry arches. Contin. Mech. Thermodyn (2014). doi:10.1007/s00161-014-0409-y
13. Ciancio, D., Carol, I., Cuomo, M.: Crack opening conditions at 'corner nodes' in fe analysis with cracking along mesh lines. Eng. Fract. Mech. **74**(13), 1963–1982 (2007)
14. Coman, C.D.: Secondary bifurcations and localisation in a three-dimensional buckling model. uZeitschrift fr Angewandte Mathematik Und Physik ZAMP **55**(6), 1050–1064 (2004)
15. Contrafatto, L., Cuomo, M., Fazio, F.: An enriched finite element for crack opening and rebar slip in reinforced concrete members. Eng. Fract. Mech. **178**(1–2), 1963–1982 (2012)
16. dell'Isola, F., D'Agostino, M,V., Madeo, A., Boisse, P., Steigmann, D.: Minimization of shear energy in two dimensional continua with two orthogonal families of inextensible fibers: the case of standard bias extension test (submitted) (2015)
17. Dell'Isola, F., Steigmann, D.: A two-dimensional gradient-elasticity theory for woven fabrics. J. Elast. **118**(1), 113–125 (2015)
18. Dos Reis, F., Ganghoffer, J.F.: Equivalent mechanical properties of auxetic lattices from discrete homogenization. Comput. Mater. Sci. **51**, 314–321 (2012)
19. D'Agostino, M.V., Giorgio, I., Greco, L., Madeo, A., Boisse, P.: Continuum and discrete models for structures including (quasi-)inextensible elasticae with a view to the design and modeling of composite reinforcements. Int. J. Solids Struct. **59**, 1–17 (2015)

20. Enakoutsa, K., Della Corte, A., Giorgio, I.: A model for elastic flexoelectric materials including strain gradient effects. Math. Mech. Solids (2015). doi:10.1177/1081286515588638
21. Eremeev, V.A., Freidin, A.B., Sharipova, L.L.: Nonuniqueness and stability in problems of equilibrium of elastic two-phase bodies. In: Doklady Physics, vol. 48, pp. 359–363. Springer, Berlin (2003)
22. Eremeyev, V.A., Pietraszkiewicz, W.: Local symmetry group in the general theory of elastic shells. J. Elast. **85**(2), 125–152 (2006)
23. Eremeyev, V.A., Pietraszkiewicz, W.: Material symmetry group of the non-linear polar-elastic continuum. Int. J. Solids Struct. **49**(14), 1993–2005 (2012)
24. Eremeyev, V.A., Lebedev, L.P.: Existence of weak solutions in elasticity. Math. Mech. Solids **18**(2), 204–217 (2013)
25. Eremeyev, V.A., Pietraszkiewicz, WojciechL Material symmetry group and constitutive equations of micropolar anisotropic elastic solids. Math. Mech. Solids (2015). doi:10.1177/1081286515582862
26. Federico, S., Grillo, A., Herzog, W.: A transversely isotropic composite with a statistical distribution of spheroidal inclusions: a geometrical approach to overall properties. J. Mech. Phys. Solids **52**(10), 2309–2327 (2004). doi:10.1016/j.jmps.2004.03.010
27. Giorgio, I., Galantucci, L., Della Corte, A., Del Vescovo, D.: Piezo-electromechanical smart materials with distributed arrays of piezoelectric transducers: current and upcoming applications. Int. J. Appl. Electromagn. Mech. (2014). doi:10.3233/JAE-140148
28. Goda, I., Assidi, M., Belouettar, S., Ganghoffer, J.F.: A micropolar anisotropic constitutive model of cancellous bone from discrete homogenization. J. Mech. Behav. Biomed. Mater. **16**, 87–108 (2012)
29. Greco, L., Cuomo, M.: B-spline interpolation of Kirchhoff–Love space rods. Comput. Methods Appl. Mech. Eng. **256**, 251–269 (2013)
30. Greco, L., Cuomo, M.: An implicit G1 multi patch B-spline interpolation for Kirchhoff–Love space rod. Comput. Methods Appl. Mech. Eng. **269**, 173–197 (2014)
31. Grillo, A., Federico, S., Wittum, G.: Growth, mass transfer, and remodeling in fiber-reinforced, multi-constituent materials. Int. J. Non-Linear Mech. **47**(2), 388–401 (2012)
32. Grillo, A., Federico, S., Wittum, G., Imatani, S., Giaquinta, G., Mićunović, M.V.: Evolution of a fibre-reinforced growing mixture. Nuovo Cimento C **32C**(1), 97–119 (2009)
33. Grillo, A., Wittum, G., Tomic, A., Federico, S.: Remodelling in statistically oriented fibre-reinforced materials and biological tissues. Math. Mech. Solids (2014). doi:10.1177/1081286513515265
34. Hilgers, M.G., Pipkin, A.C.: Elastic sheets with bending stiffness. Q. J. Mech. Appl. Math. **45**(1), 57–75 (1992)
35. Hilgers, M.G., Pipkin, A.C.: Energy-minimizing deformations of elastic sheets with bending stiffness. J. Elast. **31**(2), 125–139 (1993)
36. Laurent, C.P., Durville, D., Mainard, D., Ganghoffer, J.-F., Rahouadj, R.: Designing a new scaffold for anterior cruciate ligament tissue engineering. J. Mech. Behav. Biomed. Mater. **12**, 184–196 (2012)
37. Laurent, C.P., Durville, D., Vaquette, C., Rahouadj, R., Ganghoffer, J.F.: Computer-aided tissue engineering: application to the case of anterior cruciate ligament repair. Biomech. Cells Tissues **9**, 1–44 (2013)
38. Laurent, C.P., Durville, D., Wang, X., Ganghoffer, J.-F., Rahouadj, R.: Designing a new scaffold for anterior cruciate ligament tissue engineering. Comput. Methods Biomech. Biomed. Eng. **13**(S1), 87–88 (2010)
39. Luongo, A., Zulli, D.: A non-linear one-dimensional model of cross-deformable tubular beam. Int. J. Non-Linear Mech. **66**, 33–42 (2014)
40. Luongo, A.: Mode localization by structural imperfections in one-dimensional continuous systems. J. Sound Vib. **155**(2), 249–271 (1992)
41. Luongo, A.: Mode localization in dynamics and buckling of linear imperfect continuous structures. Nonlinear Dyn. **25**(1-3), 133–156 (2001)
42. Madeo, A., Neff, P., Ghiba, I.-D., Placidi, L., Rosi, G.: Wave propagation in relaxed micromorphic continua: modeling metamaterials with frequency band-gaps. Contin. Mech. Thermodyn. **27**(4-5), 551–570 (2013)
43. Madeo, A., Placidi, L., Rosi, G.: Towards the design of metamaterials with enhanced damage sensitivity: second gradient porous materials. Res. Nondestruct. Eval. **25**(2), 99–124 (2014)
44. Naumenko, K., Eremeyev, V.A.: A layer-wise theory for laminated glass and photovoltaic panels. Compos. Struct. **112**, 283–291 (2014)
45. Neff, P., Ghiba, I.-D., Madeo, A., Placidi, L., Rosi, G.: A unifying perspective: the relaxed linear micromorphic continuum. Contin. Mech. Thermodyn. 639–681 (2014). doi:10.1007/s00161-013-0322-9
46. Nikopour, H., Selvadurai, A.P.S.: Torsion of a layered composite strip. Compos. Struct. **95**, 1–4 (2013); cited By 0
47. Nikopour, H., Selvadurai, A.P.S.: Concentrated loading of a fibre-reinforced composite plate: experimental and computational modeling of boundary fixity. Compos. Part B: Eng. **60**, 297–305 (2014); cited By 1
48. Placidi, L., Hutter, K.: An anisotropic flow law for incompressible polycrystalline materials. Zeitschrift Fur Angewandte Mathematik Und Physik **57**, 160–181 (2006)
49. Placidi, L., Hutter, K.: Thermodynamics of polycrystalline materials treated by the theory of mixtures with continuous diversity. Contin. Mech. Thermodyn. **17**, 409–451 (2006)

50. Placidi, L., Greve, Ralf, Seddik, H., Faria, S.H.: Continuum-mechanical, anisotropic flow model, based on an anisotropic flow enhancement factor. Contin. Mech. Thermodyn. (2010) **22**, 221–237. The results obtained in this paper have been used in the entire PhD thesis of Dr. Seddik at the Low Temperature Institute in Sappore, Japan
51. Piccardo, G., D'Annibale, F., Zulli, D.: On the contribution of Angelo Luongo to Mechanics: in honor of his 60th birthday. Contin. Mech. Thermodyn. (2014). doi:10.1007/s00161-014-0388-z
52. Piccardo, G., Ranzi, G., Luongo, A.: A complete dynamic approach to the generalized beam theory cross-section analysis including extension and shear modes. Math. Mech. Solids **19**(8), 900–924 (2014)
53. Piccardo, G., Ranzi, G., Luongo, A.: A direct approach for the evaluation of the conventional modes within the gbt formulation. Thin-Walled Struct. **74**, 133–145 (2014)
54. Pipkin, A.C.: Plane traction problems for inextensible networks. Q. J. Mech. Appl. Math. **34**(4), 415–429 (1981)
55. Pipkin, A.C., Rivlin, R.S.: Minimum-weight design for pressure vessels reinforced with inextensible fibers. J. Appl. Mech. **30**(1), 103–108 (1963)
56. Pipkin, A.C., Rogers, T.G.: Plane deformations of incompressible fiber-reinforced materials. J. Appl. Mech. **38**(3), 634–640 (1971)
57. Pipkin, A.C., Rogers, T.G.: Infinitesimal plane wrinkling of inextensible networks. J. Elast. **17**(1), 35–52 (1987)
58. Pipkin, A.C.: Stress analysis for fiber-reinforced materials. Adv. Appl. Mech. **19**, 1–51 (1979)
59. Pipkin, A.C.: Equilibrium of Tchebychev nets. In: The Breadth and Depth of Continuum Mechanics, pp. 287–303. Springer, Berlin (1986)
60. Placidi, L.: A variational approach for a nonlinear 1-dimensional second gradient continuum damage model. Contin. Mech. Thermodyn. Published online 20 February 2014. doi:10.1007/s00161-014-0338-9
61. Placidi, L., Rosi, G., Giorgio, I., Madeo, A.: Reflection and transmission of plane waves at surfaces carrying material properties and embedded in second-gradient materials. Math. Mech. Solids **19**(5), 555–578 (2014)
62. Placidi, L.: A variational approach for a nonlinear 1-dimensional second gradient continuum damage model. Contin. Mech. Thermodyn. **27**(4-5), 623–638 (2014)
63. Placidi, L., Giorgio, I., Della Corte, A., Scerrato, D.: Euromech 563 cisterna di latina 17–21 march 2014 generalized continua and their applications to the design of composites and metamaterials: a review of presentations and discussions. Math. Mech. Solids (2015). doi:10.1177/1081286515576948
64. Rinaldi, A., Placidi, L.: A microscale second gradient approximation of the damage parameter of quasi-brittle heterogeneous lattices. J. Appl. Math. Mech. **94**(10), 862–877 (2013)
65. Rivlin, R.S.: Plane strain of a net formed by inextensible cords. J. Ration. Mech. Anal. **4**(6), 951–974 (1955)
66. Rivlin, R.S.: Networks of inextensible cords. In: Collected Papers of RS Rivlin, pp. 566–579. Springer, Berlin (1997)
67. Rivlin, R.S.: Plane strain of a net formed by inextensible cords. In: Collected Papers of RS Rivlin, pp. 511–534. Springer, Berlin (1997)
68. Rogers, T.G.: Crack extension and energy release rates in finitely deformed sheets reinforced with inextensible fibres. Int. J. Solids Struct. **18**(8), 705–721 (1982)
69. Sanchez-Moya, V., Pipkin, A.C.: Energy release rate for cracks in ideal composites. Int. J. Solids Struct. **13**(6), 571–578 (1977)
70. Sanchez-Moya, V., Pipkin, A.C.: Crack-tip analysis for elastic materials reinforced with strong fibres. Q. J. Mech. Appl. Math. **31**(3), 349–362 (1978)
71. Scerrato, D., Giorgio, I., Della Corte, A., Madeo, A., Limam, A.: A micro-structural model for dissipation phenomena in the concrete. Int. J. Numer. Anal. Meth. Geomech. (2015). doi:10.1002/nag.2394
72. Scerrato, D., Giorgio, I., Madeo, A., Limam, A., Darve, F.: A simple non-linear model for internal friction in modified concrete. Int. J. Eng. Sci. **80**, 136–152 (2014)
73. Selvadurai, A.P.S.: Bridged defects in uni-directionally-reinforced composites (2014); cited By 0
74. Selvadurai, A.P.S.: Bridged defects in continuously and discretely reinforced solids. J. Eng. Math. (2015); cited By 0; Article in Press
75. Selvadurai, A.P.S., Nikopour, H.: Transverse elasticity of a unidirectionally reinforced composite with an irregular fibre arrangement: experiments, theory and computations. Compos. Struct. **94**(6), 1973–1981 (2012); cited By 7.
76. Selvadurai, A.P.S., Nikopour, H.: Uniform loading of a cracked layered composite plate: experiments and computational modelling. Comput. Model. Eng. Sci. **85**(3), 279–297 (2012); cited By 5
77. Seppecher, P., Alibert, J.-J., dell'Isola, F.: Linear elastic trusses leading to continua with exotic mechanical interactions. In: Journal of Physics: Conference Series, vol. 319, p. 012018 (2011). IOP Publishing
78. Steigmann, D.J.: Two-dimensional models for the combined bending and stretching of plates and shells based on three-dimensional linear elasticity. Int. J. Eng. Sci. **46**(7), 654–676 (2008)
79. Steigmann, D.J.: A concise derivation of membrane theory from three-dimensional nonlinear elasticity. J. Elast. **97**(1), 97–101 (2009)
80. Steigmann, D.J.: Refined theory for linearly elastic plates: laminae and laminates. Math. Mech. Solids (2011). doi:10.1177/1081286511419971

81. Steigmann, D.J., dell'Isola, F.: Mechanical response of fabric sheets to three-dimensional bending, twisting, and stretching. Acta Mech. Sinica 1–10
82. Turco, E., Aristodemo, M.: A three-dimensional B-spline boundary element. Comput. Methods Appl. Mech. Eng. **155**, 119–128 (1998)
83. Wang, W.-B., Pipkin, A.C.: Inextensible networks with bending stiffness. Q. J. Mech. Appl. Math. **39**(3), 343–359 (1986)
84. Yang, Y., Ching, Y., Misra, A.: Higher-order continuum theory applied to fracture simulation of nano-scale intergranular glassy film. J. Nanomech. Micromech. 1, 60–71 (2011)
85. Yang, Y., Misra, A.: Higher-order stress-strain theory for damage modeling implemented in an element-free galerkin formulation. Comput. Model. Eng. Sci. **64**, 1–36 (2010)
86. Yeremeyev, V.A., Freidin, A.B., Sharipova, L.L.: The stability of the equilibrium of two-phase elastic solids. J. Appl. Math. Mech. **71**(1), 61–84 (2007)

Francesco dell'Isola
Dipartimento di Ingegneria Strutturale e Geotecnica
Università di Roma 'La Sapienza'
00184 Rome
Italy
e-mail: francesco.dellisola.memocs@gmail.com

Francesco dell'Isola, Tomasz Lekszycki and Leopoldo Greco
International Research Center for the Mathematics and Mechanics of Complex Systems (MeMoCS)
Università dell'Aquila
Cisterna di Latina
Italy

Tomasz Lekszycki
Warsaw University of Technology
85 Narbutta
02-524 Warsaw
Poland

Marek Pawlikowski, Roman Grygoruk
Institute of Mechanics and Printing
Warsaw University of Technology
85 Narbutta
02-524 Warsaw
Poland

(Received: June 17, 2015 ; revised: June 2[illegible], 2016)